applied sciences

MDPI

Article

Laser Ablation ICP-MS Analysis of Chemically Different Regions of Rat Prostate Gland with Implanted Cancer Cells

Anna Ruszczyńska [1], Dorota Skrajnowska [2], Agata Jagielska [1,*], Barbara Bobrowska-Korczak [2] and Barbara Wagner [1]

[1] Biological and Chemical Research Centre, Faculty of Chemistry, University of Warsaw, Zwirki i Wigury 101, 02-089 Warsaw, Poland; aruszcz@chem.uw.edu.pl (A.R.); barbog@chem.uw.edu.pl (B.W.)
[2] Department of Bromatology, Faculty of Pharmacy with the Laboratory Medicine Division, Medical University of Warsaw, Banacha 1, 02-097 Warsaw, Poland; dskrajnowska@wum.edu.pl (D.S.); barbara.bobrowska@wum.edu.pl (B.B.-K.)
* Correspondence: ajagielska@chem.uw.edu.pl

Abstract: The comparison of tissues analyzed by LA-ICP-MS is challenging in many aspects, both medical and mathematical. The concept of distinguishing regions of interest (ROIs) was proposed in the literature, allowing for data reduction and targeted comparative analysis. ROIs can be drawn before any analysis, by indicating the anatomical parts of tissue, or after the first step of analysis, by using elemental distribution maps and characteristic regions of enrichment in selected elements. A simple method for identifying different regions, without the manual extraction of image fragments, is highly needed in biological experiments, where large groups of individuals (with samples taken from each of them) is very common. In the present study, two ROIs were distinguished: (1) tissue-rich in fat (and tissue-poor in water); and (2) tissue-rich in water (and tissue-poor in fat). ROIs were extracted mathematically, using an algorithm based on the relationship between ^{13}C and ^{23}Na signal intensities. A cut-off point was indicated in the point of the simultaneous decrease in ^{13}C and increase in ^{23}Na signal intensity. Separate analyses of chemically different ROIs allow for targeted comparison, which is a great advantage of laser ablation over liquid introductions to ICP-MS. In the present experiment, tissues were provided from animals with implanted prostate cancer cells as well as supplemented with mineral compounds particularly important both for prostate gland functions (Zn and Se) and neoplastic processes (Ca, Fe, and Cu). One of the goals was to try to determine whether dietary supplementation qualitatively and quantitatively affects the mineral composition of the prostate gland.

Keywords: laser ablation; ICP-MS; ROI; prostate gland; prostate cancer

check for updates

Citation: Ruszczyńska, A.; Skrajnowska, D.; Jagielska, A.; Bobrowska-Korczak, B.; Wagner, B. Laser Ablation ICP-MS Analysis of Chemically Different Regions of Rat Prostate Gland with Implanted Cancer Cells. *Appl. Sci.* **2022**, *12*, 1474. https://doi.org/10.3390/app12031474

Received: 21 December 2021
Accepted: 26 January 2022
Published: 29 January 2022

Publisher's Note: MDPI stays neutral with regard to jurisdictional claims in published maps and institutional affiliations.

Copyright: © 2022 by the authors. Licensee MDPI, Basel, Switzerland. This article is an open access article distributed under the terms and conditions of the Creative Commons Attribution (CC BY) license (https://creativecommons.org/licenses/by/4.0/).

1. Introduction

1.1. Chemical Analysis of a Prostate Gland

Prostate cancer is the most common malignancy in men, and the morbidity has a tendency to increase. Moreover, over the past decade, reductions in prostate cancer mortality rates have ceased [1,2]. There are three well-established risk factors: age, race/ethnicity, and family history related to inherited genetic factors [3,4]. Due to the slow progression and low latency period of this type of malignancy, lifestyle factors are also investigated. Although dietary factors (such as energy intake [5], saturated fatty acids, trans-isomers, n-3 fatty acids [6], calcium [7], selenium, vitamin E [8], vitamin D [9]) were studied, no clear recommendation could be listed apart from the facts versatile for all cancers prevention [10]. Dietary factors can modify elemental metabolism before the occurrence of morphological signs of disease, focusing attention on chemical alterations apart from histopathological changes in tissues. Particular regions of structure and chemical composition can be distinguished within the prostate gland, e.g., the peripheral zone, rich in specialized zinc-accumulating cells responsible for citrate production and secretion [11].

Peripheral and transitional zones of the cancerous prostate gland differed in Se and selenomethionine contents, and these species were quantified by means of high-performance liquid chromatography coupled to ICP-MS [12]. Doble et al. [13] used laser ablation inductively coupled plasma mass spectrometry (LA-ICP-MS) to inspect the general Mn content in prostate tissue. High-resolution laser ablation imaging of Zn distribution [14] enabled quantification of this element in the prostate gland. Visible boundaries between the healthy and cancerous tissue rich in Zn were observed [14]. Different instrumental techniques were used in order to measure the total content or comparison of elemental distribution, including: flame atomic absorption spectrometry [15], neutron activation analysis [16,17], inductively coupled plasma mass spectrometry (ICP-MS) [16,17], and total reflection X-ray fluorescence [18]. Increased mass fractions of several elements with age, as well as specific ratio modifications in individuals with cancer, were found in the cited studies [16,17].

1.2. Mineral Compounds in Prostate Gland Cancer

Chronic diseases, especially cancer, disturb organisms' homeostasis. This is also clearly visible in the content of minerals, which plays an important role in biochemical and metabolic processes in serum and organs. An excess or deficiency of micronutrients may contribute to the development of neoplasms, and sometimes, the dependence can be the opposite: changes in chemical composition may result from the properties of neoplasm. Taking into account changes in the concentrations of elements, the gene profiles of the transporting factors of some of them can be used as biomarkers for the early detection and risk assessment of neoplastic diseases [19,20]. Many researchers have tried to find relationships between cancer and the abnormal contents of elements in diseased tissue. In some cases, a direct link has been found between changes in the content of mineral components and the disease as such or, more specifically, its duration or stage [19,21]. In some cases, the observed differences were secondary and did not represent a true cause-and-effect relationship. Even then, however, they might have prediction value [19,21–27].

Among many bioelements taken with food or in the form of supplements, Se, Zn, Cu, Fe, and Ca play a special role. It was noticed that regardless of the type of cancer and its advancement, the level of Se in tissues and blood decreases if compared with healthy people. It is related to decreased glutathione peroxidase activity and antioxidant properties [28]. The incidence of prostate, breast, lung and stomach cancer has been shown to be strongly correlated with low plasma selenium levels [28,29]. Some selenium compounds are involved in the mechanisms of programmed cell death (PCD). PCD impairment is one of the major processes during cancer progression [30]. Selenium inhibits the uncontrolled growth of cancer cells [31]. Appropriate concentrations of selenium compounds, inhibiting the G1, G2 and S phases of the cell cycle, prevent the carcinogenesis [32]. On the other hand, the effect of selenium is closely related to the dose–response relationship. Selenium supplementation, if its level is already elevated in the organism, may lead to tumor growth. Free oxygen radicals, hydrogen peroxide, and organic peroxides damage genetic material and thus contribute to the development of cancer. Glutathione peroxidase protects against protein and DNA degradation by maintaining the balance between these compounds [33]. Many studies indicate a high concentration of selenium in tumor tissues, which hypothetically may be the reason for its deficiency in disease [33]. Undoubtedly, the level of selenium in the blood may be a sensitive marker of the risk of cancer, but the current health condition and genetic conditions should be taken into account, according to which the optimal level of individual micro- and macroelements must be determined individually. Cell cycle control disorders caused by differences in calcium ion concentrations may be crucial for neoplastic transformations [34]. Calcium, due to its influence on the insulin-like growth factor (IGF) system, influences the formation of prostate cancer. IGF-1 has a mitogenic and anti-apoptotic effect on normal and transformed prostate epithelial cells. In the development of tumors, an increase in the release of parathyroid hormone (PTH) and 1,25-dihydroxyvitamin D can be noticed, which causes an increased level of calcium in the blood. Calcium homeostasis is maintained by the calcium receptor (CaR). It

is "specifically" sensitive to the detection of extracellular calcium levels. It is also involved in changes in PTH secretion and calcium reabsorption in the kidneys. Studies indicate that CaR may be a mediator of the calcium-initiated extracellular effects on prostate cancer cells, due to the association of receptor expression in tumor cells with the proliferative effect of increased extracellular calcium and cell metastasis [35,36]. Many epidemiological studies have tried to link the consumption of a calcium-containing diet to the risk of various types of cancer, especially prostate cancer [36,37]. Literature data from scientific studies confirm the existence of a relationship between the amount of calcium consumed and the development of neoplastic disease. Most studies focused on the beneficial effects of calcium on the risk of colorectal cancer [38]. This is probably due to the formation of insoluble soaps with bile acids in the lumen of the large intestine. Contrary to the data for colorectal cancer, data for prostate cancer are inconsistent [35]. It is believed that iron can promote cancer development by generating reactive oxygen species, damaging, e.g., DNA, contributing to cell damage, mutation, or death. Other mechanisms are: increasing inflammation, stimulating angiogenesis, and acting as a nutrient for cancer cells [39]. In patients with chronic diseases and cancer, iron levels are often low, and iron regulation and homeostasis are disturbed. Cancer cells accumulate iron. Most patients have functional iron deficiency (FID). Even if the level is adequate, there can be problems with the supply of this element to erythroblasts and other iron-dependent tissues. FID is a consequence of the release of tumor-associated cytokines. The phenomenon of anemia in chronic diseases may exacerbate symptoms and increase mortality due to neoplastic disease [40]. Anemia is associated with the upregulation of hepcidin, which is induced by BMP2 (bone morphogenetic protein) in myeloma and interleukin 6 (IL-6) in Hodgkin's lymphoma. In many tumors, activity of the transcription factor HIF (hypoxia inducible factor) increases, which is involved in the regulation of iron levels. HIF is activated by hypoxia, which increases iron uptake, and may contribute to the accumulation of the element in cancerous tissues. This mechanism is one of the causes of disease progression [41]. It has been shown that in prostate cancer, the level of ferroportin (Fpn) is reduced compared with healthy tissues [42]. Research also confirms a strong correlation between iron deficiency and elevated levels of calcium and magnesium in cancer patients [43]. Increased levels of copper in serum and tumors have been observed in many malignant neoplasms, such as breast, ovarian, lung, and stomach cancer. It has also been shown to be strongly associated with tumor progression and relapse [44,45]. In the case of prostate cancer, Cu concentrations are rather normal, regardless of the disease stage. This is true for both serum copper and its accumulation in tumor tissues [45]. The reason for the increase in copper levels in neoplastic tissues is unknown. It is known, however, that this results in increased angiogenesis. Tumor growth and progression depend on angiogenesis and neovascularization processes, which require the presence of growth factors, proteases, and copper. Copper is a cofactor of these processes; therefore, its high concentration is essential in cancer cells [44]. Based on this phenomenon, a thesis was drawn that active inhibitors of the copper proteasome complex can not only inhibit angiogenesis, but also induce the apoptosis of cancer cells [45].

All these specific mechanisms for every element participation in the carcinogenesis process were the reason for choosing such a set of analytes in the presented study.

1.3. ROI Concept

The ROI conception was proposed in the literature to prevent losing some information after averaging the analytical signal from an area which resulted in bulk analysis only. The initialism ROI means "region of interest" and signifies a carefully selected part of the sample. Such areas can be treated as an integrity and often analyzed as a whole, despite the collection of more detailed data. Distinctions of ROIs are performed either before the analysis by the separation of anatomical or histological parts of the tissue, or after analysis, e.g., if elemental distribution maps indicate particulate areas.

The nervous system is the main biological sample which is either divided into ROIs or only selected ROIs are subjected to analysis. Rao et al. [46] distinguished three ROIs in

mouse brains (entire hemisphere, hippocampus, and cortex) by manual extraction with the use of a copper distribution map. Maximum copper contents located along the ventricles identified the edges. The mouse brain was also in the field of interest for Matusch et al. [47] in the context of neurodegenerative disease that can influence the very local distribution of elements. Based on the previously published "The Mouse Brain in Stereotaxic Coordinates" atlas [48] and comparison of elemental distribution maps (Zn, Cu, Fe, Mn, C, and P) with histological image after cresyl violet staining, the researchers [47] covered the whole brain section area with ROIs. If absolute calibration was not possible, signal intensities were normalized to the average of the reference region, which was the corpus callosum for the most of elements. Univariate one-way analysis of variance (ANOVA) was used to compare group means, and some statistically significant differences were found, especially in the periventricular zone and interpeduncular nucleus between the control group and those treated with MPTP (inducing Parkinson's disease) [47]. Opačić et al. [49] selected ROIs as coronal sections, as described elsewhere by Duvernoy et al. [50]. Fingerhut et al. [51] analyzed Gd concentrations in brain tissue and distinguished two main ROIs: (1) the dentate nucleus (DN), divided afterwards into four more detailed parts, although still treated as a single ROI; and (2) the surrounding region. Separate Gd contents in each ROI determined by LA-ICP-MS strongly differed from the total content quantified by ICP-MS with solution nebulization, which confirmed use of targeted analyses of a solid sample [51]. The authors stated that the Gd content may vary considerably, even between two adjacent laser spots [51].

The second well-known LA-ICP-MS-supported medical area is metal-containing xenobiotic analysis. Imaging of Pt in thin layers of blood cells taken from patients treated with cisplatin performed with LA-ICP-MS was advantageous in view of short analyses and simple sample preparation. Blood cell thin films were stained in order to find the ROIs containing white blood cells; thus, in this case, ROIs were selected before the laser ablation [52]. In Kamaly et al.'s study [53], histopathological analysis indicated the ROI, which was separated by drawing a line around the tumor surface. Then, targeted Gd analysis was possible, showing the distribution of Gd-containing contrast agents. Radbruch et al. [54] proposed the statistical use of ROIs on the example of Gd deposition from GBCA–gadolinium-based contrast agents. The authors identified the area of DCN (deep cerebellar nuclei) by the increased ^{57}Fe transient signals. The mean Gd concentration in the DCN was calculated by averaging the data obtained from three ROIs of the approximate area 880 µm × 880 µm and of 500 data points each. Similarly, three regions of interest outside the DCN were selected for averaging the Gd concentration in the surrounding tissue [54]. Bücker et al. [55] analyzed the iatrogenic gadolinium as well as lanthanum (from lanthanum carbonate) deposition patterns. The authors described the use of ROIs for the representative statistical analysis of quantitative results. Five ROIs (250 µm × 250 µm) were designated over all tissue of the same type (mainly in the kidney and cerebellum), avoiding special structures such as vessels. Small special structures were analyzed separately, with adapted ROI sizes. The elemental content was calculated by averaging the content quantified in all ROIs of the same type. The main deposition of both elements was found in the middle coat of blood vessels in a ring-like shape, which was clearly visible in the published LA-ICP-MS images [55]. Uca et al. [56] predefined ROIs in atherosclerotic plaque using an SR-µXRF method. Then, the authors investigated the selected region by LA-ICP-MS toward Gd from contrast agents. The method of LA-ICP-MS achieved a better resolution and found small areas of high Gd content. Sajnóg et al. [57] also analyzed the atherosclerotic lesions and divided the obtained material into four ROIs: (1) atherosclerotic plaque; (2) connection between the atherosclerotic plaque and the arterial wall; (3) outer wall; and (4) the inner wall or fibrous cap on the atherosclerotic lesion. A photograph of the sample taken prior to ablation enabled drawing the ROIs with the imaging software tools. The boundaries of each ROI were delineated so that they did not touch each other and were placed in the central part of the sample. This approach for ROI extraction ensured the covering of only one type of region of the sample and avoiding overlapping with the plastic base. The connection

between the atherosclerotic plaque and the arterial wall was described by the authors as a smooth transition between the arterial wall (representing soft tissue) and the atherosclerotic plaque. In some cases, two areas were treated as a single ROI, when it was possible to find them in two different localizations (e.g., the connection between the atherosclerotic plaque and the arterial wall). ROIs could be well distinguished due to the sharp boundaries of high signal intensities for selected elements in plaque and for other elements in the arterial walls [57]. The term "ROI" in LA-ICP-MS measurements can be found also in M.-M. et al.'s two studies published in 2013 [58,59]. The authors described ROIs as "freely drawn" and calculated the average content of trace metals separately for each region; in this case, of a human liver.

One of the directions of LA-ICP-MS development is designing software which would simplify handling LA-ICP-MS data and, at the same time, allow for easy ROI extraction. Castellanos-Garcia et al. [60] proposed dedicated software based on Python programming language that uses more advanced segmentation algorithms for ROI classifications.

In 2011, Osterholt et al. [61], while presenting their new software (IMAGENA), proposed the identification of free-hand-drawn ROIs, including the glass or other blank background outside the sample and areas based on anatomical criteria inside. Halbach et al. [62] proposed dedicated software, FishImager, to assign a biological feature as an ROI and overlay it with a quantitative LA-ICP-MS image. Phenotypic features were identified with the corresponding software, FishInspector, based on a microscopic image and automatically defined as biological ROIs. For each ROI, descriptive statistics such as the sum, mean, standard deviation, median, variance, minimum, and maximum were calculated. Different cluster algorithms could also be applied to the LA-ICP-MS data; then, cluster data could be correlated with the ROIs. Combination of biological ROIs with the cluster results was very important, as it enabled the move from visual observations and interpretations towards validation and statistical proof. The authors applied this described use of software tools to a study focused on zebrafish embryos, with three main goals: (1) the distribution analysis of natural elements (based on ^{12}C, ^{39}K, and ^{31}P isotopes) and the reproducibility between ablations of different individuals; (2) finding the accumulation zones of iodine- and bromine-containing xenobiotics; and (3) analyzing the influence of the exposure time and developmental stage on the uptake and distribution of xenobiotics. Addressing all of the above-mentioned questions was possible because of the proposed tools [62].

Despite several examples described in the literature, it can be seen that the ROI concept is neither well established nor widely used. In 2020, Castellanos-García et al. [60] called extracting ROIs a "more sophisticated image processing method". In their review, Lee et al. [63] mention ROIs only in the context of SIMS, even though LA-ICP-MS is described as one of the methods to study metal-based drug distributions in different biological systems. In their review from 2014, Becker et al. [64] summarize the data treatment in few steps: (1) the reconstruction of a two-dimensional map in dedicated software from the raw data; (2) the selection of ROIs (the whole sample or anatomically selected areas) and compulsorily the background; and (3) averaging the information from each ROI. The authors do not define how to delineate ROIs. Basing on the other publications from Becker's group, it can be assumed that they are extracted manually (ROIs are described as "freely drawn" in the software) [47,58,59,65,66]. This group also called partitioning the tissue into ROIs "segmentation" [67]. The same authors describe more precise alternatives to the extraction of relatively large ROIs, i.e., comparing every single pixel with magnetic resonance, or maybe simply microscopic images. However, significant deformations occur during the slicing process that may influence the exact position of microscopic fragments [67]. Great advantages of image segmentation for ROIs have been emphasized by many authors [47,60]. The differentiation of histologically relevant fragments of a tissue is valuable for understanding the essential biochemical and biological processes [60]. Moreover, data concerning small substructures may be lost if the entire ablated area is analyzed together or, even worse, bulk analysis is applied [47].

In the most of the cited papers, ROIs were extracted manually; however, the support of automated and objective procedures is described as desirable [67]. It is emphasized that dividing the sample into ROIs is valuable, especially for group comparisons [67]. Individual ROIs should correspond to the anatomical structures and should be as homogeneous as possible. Depending on the aim of a study, divisions can be executed on a finer or a coarser scale [67]. In our study, a mathematical approach to distinguish two regions was proposed, in order to find more universal and simple method of data analysis.

2. Materials and Methods

2.1. Biological Material

Male Sprague Dawley rats (n = 70) were obtained from the Animal Laboratory, Department of General and Experimental Pathology from the Medical University of Warsaw. The study was approved by the Ethics Committee, Medical University of Warsaw (protocol code 45/2014, date of approval 15 April 2014). Tested animals were housed in standard conditions with a 12 h light–dark cycle at 22 °C. Rats were fed with a standard diet (Labofeed H, Kcynia, Poland) and water ad libitum. The diet contained the following compounds (per 1 kg): protein (210 g), fat (39.2 g), fiber (43.2 g), ash (55 g), carbohydrates (300 g), vitamin A (15,000 IU), vitamin D3 (1000 IU), vitamin E (90 mg), vitamin K3 (3 mg), vitamin B1 (21 mg), vitamin B2 (16 mg), vitamin B6 (17 mg), vitamin B12 (80 µg), pantothenic acid (30 mg), folic acid (5 mg), nicotinic acid (133 mg), Ca (10 g), P (8.17 g), Mg (3 g), K (9.4 g), Na (2.2 g), Cl (2.5 g), S (1.9 g), Fe (250 mg), Mn (100 mg), Zn (76.9 mg), Cu (21.3 mg), Co (2.0 mg), I (1.0 mg), and Se (0.5 mg).

2.2. Experimental Procedure

The experiment was carried out for 90 days. After a 10-day adaptation period (from rat ages of 60 to 70 days), animals were randomly divided into an experimental group (those with implanted prostate cancer cells) and control group (those without cancer cells). The control group was accommodated under the same conditions as the experimental group and fed with the same diet. The cancer cells (LNCaP) were implanted intraperitoneally into the rats at the 90th day of their lifetime in amounts of 1×10^6 in 0.4 mL of phosphate-buffered saline. The certified line of androgen-dependent human prostate cancer cells was obtained from ATCC Bank (American Type Culture Collection, Menassas, VA, USA). Experimental and control animals were divided into dietary groups and supplemented with minerals by oral gavage (Table 1).

Table 1. Dietary group characteristics. The number of samples from each group is specified in the first column (n). One half of the samples in each dietary group represents the experimental group with implanted cancer cells, whereas the second half represents the control group, except for the Ca and Standard groups, where the division was 5(ctrl) + 6(exp).

Dietary Group	Concentration of Element/g·L^{-1}	Dose of Element/mg/Day/Rat	Chemical Form in Aqueous Suspension
Zn-suppl (n = 12)	4.6	1.85	$ZnSO_4 \cdot 7H_2O$
Cu-suppl (n = 12)	0.639	0.256	$CuSO_4 \cdot 5H_2O$
Se-suppl (n = 14)	0.018	0.0072	Na_2SeO_4
Fe-suppl (n = 10)	7.5	3.0	$FeSO_4 \cdot 7H_2O$
Ca-suppl (n = 11)	75	30	$CaCl_2 \cdot 6H_2O$
Standard (n = 11)	-	-	-

The rats were fed with 0.4 mL of supplemented suspension daily, from the 70th until 150th day of their lifetime. The animals fed only with the standard diet (without supplementation) received 0.4 mL of water. The doses of trace elements were selected

based on the values used in the Labofeed H diet. According to the level of trace elements in the Labofeed diet, the rats were fed, via gavage, extra supplements of the following: double doses of Zn and Cu, one dose of Fe, or a quarter dose of Ca. The doses of selected minerals were chosen based on their levels in dietary supplements for humans.

2.3. Instrumentation

Samples were dried in an SLN 240 drying oven (Pol-Eko, Wodzisław Śląski, Poland). The measurements were carried out using a quadrupole ICP-MS instrument (Nexion 300D, Perkin Elmer Sciex, Waltham, MA, USA), coupled with a laser ablation system (LSX 213, Cetac Technologies, Omaha, NE, USA). Instrumental conditions are shown in Table 2. Results from LA-ICP-MS measurements were compared with a previously published study [68] concerning ICP-MS analyses, with solution nebulization-working parameters also cited in Table 2.

Table 2. LA-ICP-MS instrumental conditions.

ICP-MS	LA-ICP-MS	ICP-MS [68]
RF power	1350 W	1350 W
Carrier gas flow rate (Ar)	0.9 L/min	0.9 L/min
Dwell time	5 ms	50 ms
Readings	12,000	3
Sweeps	1	1
Replicates	1	3
Monitored isotopes:	^{13}C, ^{23}Na, ^{26}Mg, ^{27}Al, ^{31}P, ^{32}S, ^{34}S, ^{35}Cl, ^{39}K, ^{44}Ca, ^{57}Fe, ^{65}Cu, ^{66}Zn, ^{78}Se, ^{88}Sr, ^{202}Hg, ^{208}Pb	^{23}Na, ^{24}Mg, ^{39}K, ^{43}Ca, ^{57}Fe, ^{63}Cu, ^{66}Zn, ^{82}Se, ^{88}Sr, ^{208}Pb
Laser Ablation		
Ablation mode	multi-line ablation	
Number of ablation lines	15	
Laser energy	0.5 mJ	
Laser shot frequency	20 Hz	
Spot size	100 µm	
Space between lines	100 µm	
Scan rate	50 µm/s	
Shutter delay	20 s	
Ablation time per sample	1020 s	

2.4. Sample Treatment

Prostate tissue collected from rats was dried in the laboratory oven (24 h, 37 °C), a method with reduced influence on the elemental composition compared with freeze-drying, which was proven in a previous study [69]. The estimated thickness was about 3 mm, which ensured that the tissue was not punctured. After ablation, this was checked using optical microscopy. Laser ablation ICP-MS was performed on each sample (i.e., each prostate gland) with 15 ablation lines, covering an area of approximately 6 mm^2, typically including two macroscopically different regions (lighter—rich in adipocytes, and darker—typical gland tissue). Total elemental contents were quantified by means of ICP-MS with solution nebulization, as described elsewhere [68].

2.5. Data Treatment

Microsoft Excel 2010 software (Microsoft, Redmond, WA, USA) with the XLSTAT add-on was used for calculations. Transient signals were registered for the selected isotopes (see Table 2) during each measurement cycle. The intensities of blank signals for carrier gas (Ar) flow rates were registered for each isotope individually for 20 s before the start of ablation. These were used to calculate the mean of the instrumental blank ($mean_{/BLANK/}$) and SD ($SD_{/BLANK/}$). $Mean_{/BLANK/}$ values were subtracted from the signals registered during ablation of the samples. Spikes, defined as single raw data intensities higher than

the means of two neighboring data values, were removed and replaced with the mean of the neighboring values. Isotope ^{13}C was selected as the internal standard (IS). Limits of quantitation (LOQ) were calculated for each element, based on the formula recommended by IUPAC [70]: $LOQ = mean_{/BLANK/} + 10SD_{/BLANK/}$; from the list of monitored isotopes (Table 2), only the information about the elements presenting signal intensities above the LOQ (C, Na, Mg, Al, P, S, Cl, K, Ca, Fe, Cu, and Zn) in all samples was subjected to further analysis. Statistical analysis was performed using analysis of variance (ANOVA), preceded by checking the normal distribution with the Shapiro–Wilk test and homoscedasticity with Levene's test. In cases of statistically significant differences (p-value below 0.05), Tukey's post hoc-test was performed in order to compare which groups differed from each other.

3. Results and Discussion

Elemental distribution maps (Figure 1) are inhomogeneous. Areas with higher fat content (brighter in the photo) are characterized by lower water content and, consequently, high signal intensity from ^{13}C (used as an internal standard) and lower intensities from typical electrolytes. Several similarities between elements can be observed: electrolytes such as Na, K, Mg, and Ca are correlated, whereas other elements demonstrate diversity—S and Fe are quite uniformly distributed in low-fat areas and in case of Cl and Zn unique enrichment areas are visible. It can be noted that ^{13}C and ^{23}Na signal intensities are negatively correlated, and two regions of interest (ROIs) were distinguished based on this observation: (1) rich in organic matter/fat and poor in water (F); and (2) rich in water and poor in organic matter (W).

As it can be seen from Figure 1, the comparison of whole ablated areas would be unreliable, due to the presence of two substantially different tissues, covering variant, irregular surface of each sample. This is why the numerical distinguishing of two ROIs was proposed. The signals were ordered as ^{13}C descending (Figure 2A,B), as described in the previous paper by Wagner and Czajka [71]. Such ordering allowed for relatively precise selection of the signal integration range. Numerical distinction of two ROIs was established for each sample based on signal intensity versus the number of data point plots ordered by the descending ^{13}C signal. A clear cut-off point could be seen, corresponding to a decrease in the signal intensity for ^{13}C and a simultaneous increase in the signal intensity for ^{23}Na (Figure 2).

All registered data (Figure 2A) were ordered as C descending (Figure 2B). A signal integration range was selected to omit the problem with variable heterogeneity of the samples and to extract the areas of the condensed chemical information from each ROI separately [71]. Signal intensities (normalized to ^{13}C as IS) from each ROI of each sample were averaged separately. Through principal component analysis, it was shown that even after excluding C from calculations, the difference between F-ROI and W-ROI was clearly visible (Figure 3). Moreover, two groups of coexisting elements can be distinguished: (1) Na, K and Cl (with similar tendency for Fe and Al); and (2) Ca, Cu, Mg, P, S, and Zn.

Average relative signal intensities from both ROIs ("W" ROI and "F" ROI) of each sample were included in further calculations. Values from the same condition group (for example: Zn-supplemented with cancer cells) were treated as biological replicates and all samples (n = 70) were subjected to the statistical analysis. Analysis of variance (ANOVA) tests were performed, preceded by checking normal distribution by Shapiro–Wilk test and homoscedasticity by Levene's test. In the case of statistically significant differences (p-value below 0.05), Tukey's post hoc test was performed in order to find which means were significantly different from each other. The condition group's results were compared for each element in order to check if cancer cell implantation and/or diet supplementation influenced the elemental content in specific regions of the prostate gland.

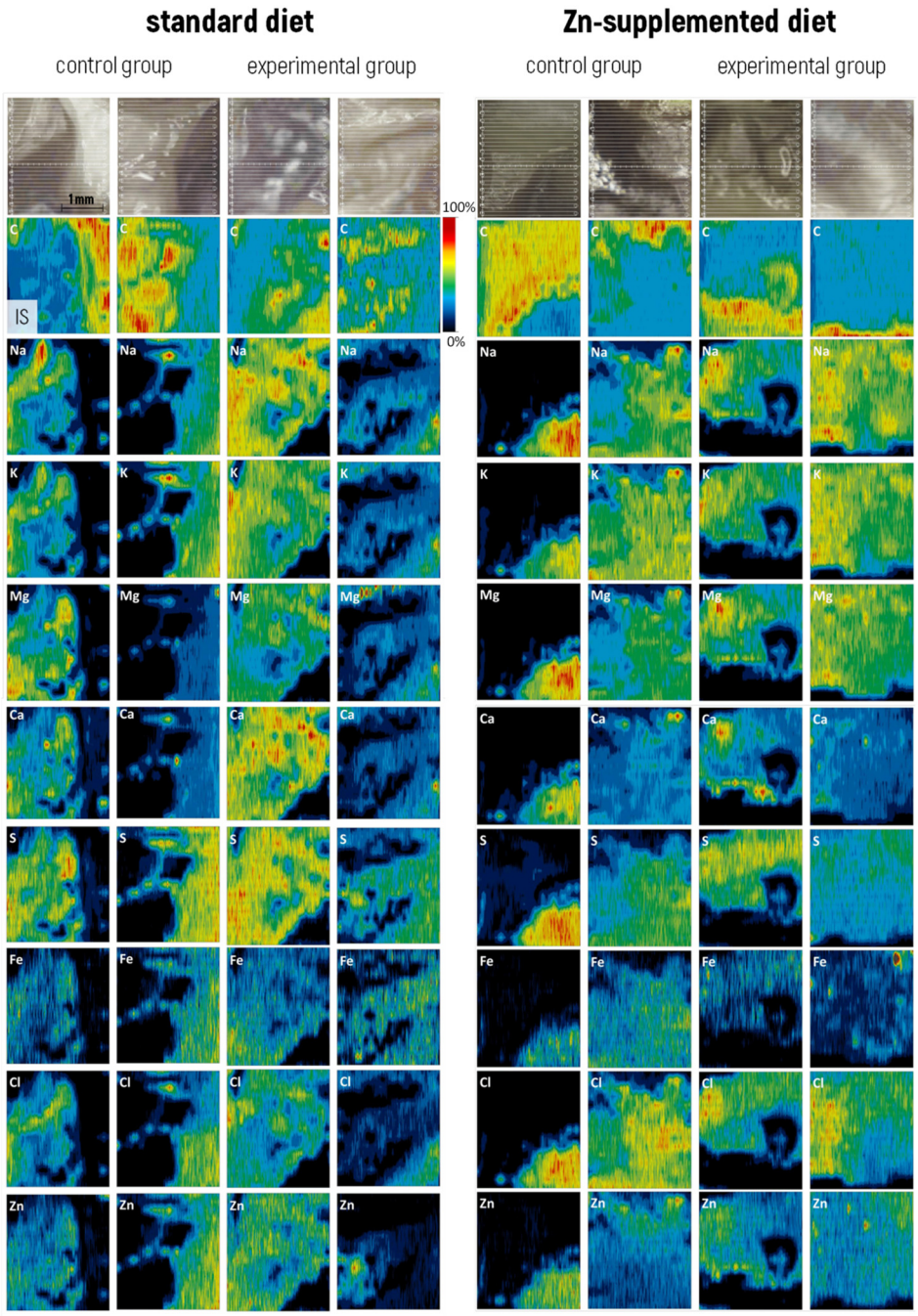

Figure 1. Elemental distribution maps of eight selected samples of the prostate gland, fed with two different diets and with (experimental) or without (control) implanted cancer cells. Each column represents the sample taken from the other animal (biological replicate). Relative signal intensities are normalized to the maximal signal for each sample and each element (100%).

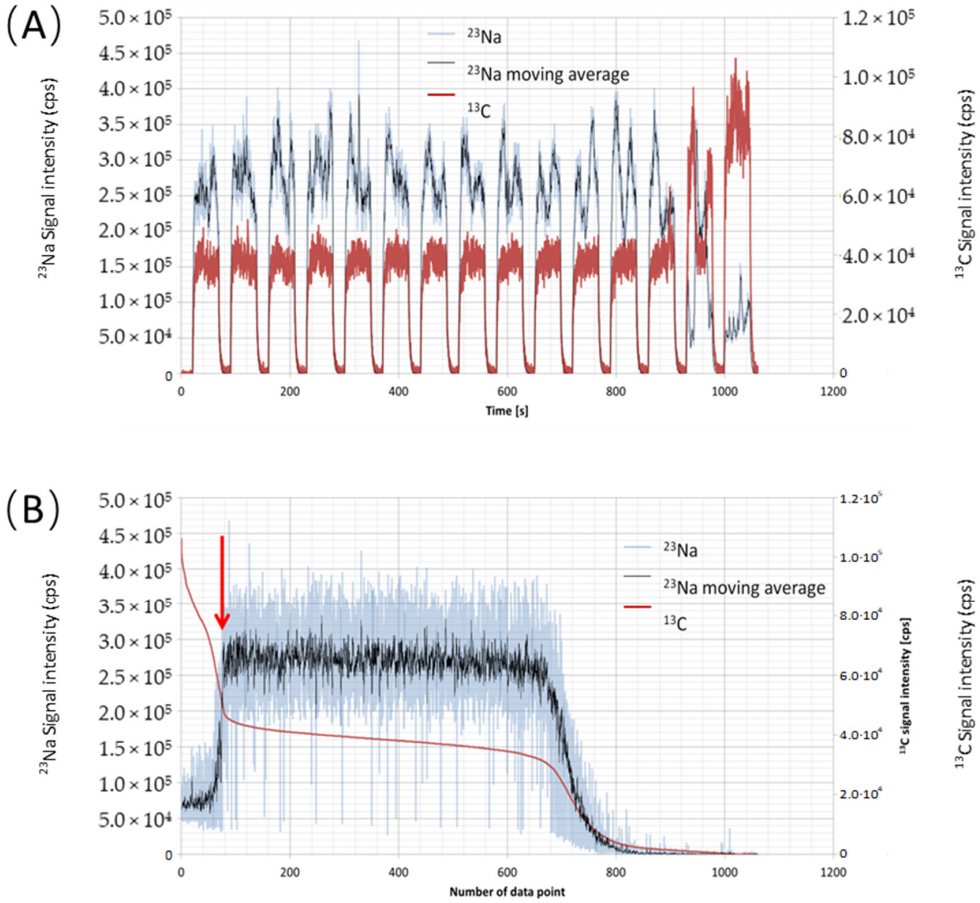

Figure 2. Signal intensity versus number of data points plotted before (**A**) and after (**B**) sorting by descending signal for isotope ^{13}C. The cut-off point between two ROIs is marked with a red arrow. Exemplary plots are presented for the same sample as in the last column in Figure 1.

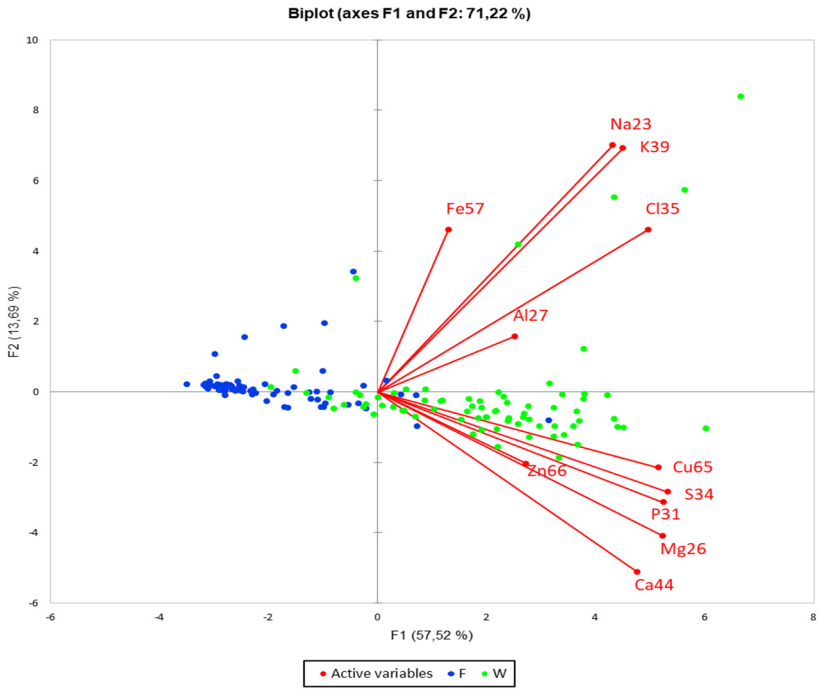

Figure 3. Biplot of averaged isotopic signal intensities in F1/F2 dimension constructed from the data of all prostate glands (n = 70), divided into rich in fat (F) and rich in water (W) parts.

Only in the case of Zn, in "W" ROI, were statistically significant differences noticed, as indicated in Figure 4A. Zinc contents in healthy prostate glands are very high, because this element is required for important prostatic functions [72]. The error bars in Figure 4 represent the differences between biological, not technical, replicates; thus, relatively high values are understandable. Standard deviation values in the case of zinc were higher than in the case of other elements, which was also observed by other authors [15] and in our previous experiment [68]. This inter-group inhomogeneity can be explained by zinc accumulation by prostate gland cells and its metabolic involvement in prostate carcinogenesis [73]. Zn contents in the prostate gland are characterized by very high individual variability [15]. Dietary supplementation with calcium, iron, copper, and selenium could weaken the absorption of zinc at the first stage in the intestinal wall, which may partially explain the effect of dietary supplementation, without such an effect for a non-supplemented, i.e., standard diet. In addition, the implantation of prostate cancer cells could exacerbate zinc deficits in the gland. In men with adenocarcinoma of the prostate, the concentration of zinc in the prostate tissue decreases significantly compared with the surrounding healthy tissues [74]. It has been noticed that the degree of malignancy of prostate cancer may be conditioned by deteriorations in the zinc content. Already in the early stage of carcinogenesis, the concentration of this microelement decreases, and with the development of a tumor, it is further reduced [74,75]. The risk of DNA damage increases, and this leads to a malignant transformation. Moreover, as the prostate epithelial cell transforms into a cancer cell, the ability to accumulate intracellular zinc is lost. In the initial stage of cancer, the expression of zinc uptake transporters in cells (ZIP- and Irt-like proteins) is also reduced, and as the disease progresses, their number continues to decline [76–78].

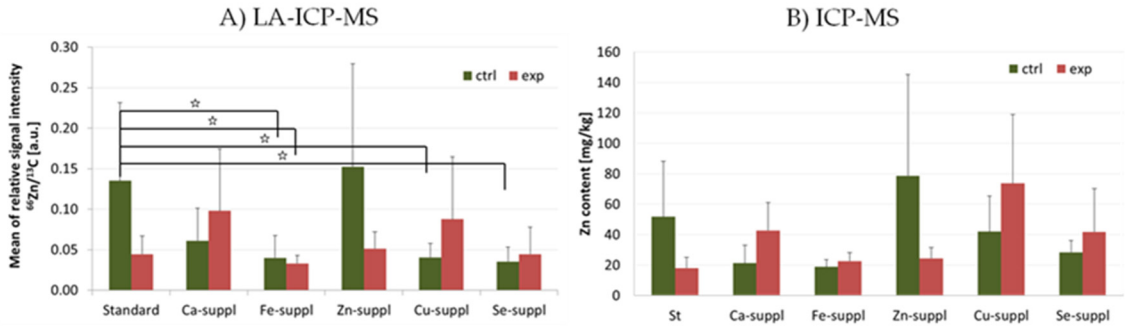

Figure 4. (**A**) Averaged relative signal intensities $^{66}Zn/^{13}C$ from "W" ROI (LA-ICP-MS analysis) compared with (**B**) Zn content in the same prostate gland samples quantified by ICP-MS with solution nebulization [68].

Distinguishing ROIs allowed for logical comparison to be drawn, even for the samples which were characterized by inhomogeneous distribution of the elements of interest (Ca, Fe, Zn, and Cu), caused, above all, by the presence of two basically different areas of the prostate gland. Samples were grouped by diet and medical intervention (prostate cancer cell implantation), and the main medical aim of the study was to identify the differences between groups. Comparing the results from bulk analysis was the first step of the study, and some differences were found; however, they did not give a definite answer about the influence of the described interventions. Therefore, more detailed analysis was planned by using LA-ICP-MS with very localized material collection.

Results obtained from LA-ICP-MS and ICP-MS analysis (with the working parameters cited in Table 2) were compared (Figure 4). Graphical distribution of the bar plot prepared only with relative signal intensities from LA-ICP-MS measurements showed high correlation in the observed tendencies with bar plots based on quantitative analysis by ICP-MS with solution nebulization after mineral digestion (Figure 4).

4. Conclusions

Distinguishing two chemically different ROIs in one sample analyzed by LA-ICP-MS is possible due to a simple mathematical operation, i.e., sorting signal intensities by descending signal intensity for the chosen isotope (here: ^{13}C) and finding cut-off points that may be the inflection point, local extremum, or another visible change in the course of the function. In the elemental distribution maps, two macroscopically different regions could be identified; importantly, they covered different areas of each sample. In biological experiments, the number of samples is usually high (here: 70); therefore, a simple method for finding different regions, without the manual extraction of image fragments, is highly needed. Separate analyses of chemically different ROIs enable targeted comparisons, which is a great advantage of laser ablation ICP-MS, compared with solution nebulization. In the LA-ICP-MS analysis with the proposed analytical scenario, significant differences were observed between Zn content in the standard sample (standard diet, without cancer cells) and a few diet groups: Fe-supplemented, Cu-supplemented, and Se-supplemented, only in the "W" ROI. The proposed protocol may be improved in the future by using machine learning tools that can reduce typical ambiguity and extract sensitive information from large datasets. Principal component analysis reductions with the uniform manifold approximation and projection (UMAP) algorithm were recently applied to large datasets [79,80] and could be produced by mass spectrometry during chemical imaging.

Author Contributions: Conceptualization of biological part, D.S. and B.B.-K.; conceptualization of chemical part, B.W.; software, A.R., A.J. and B.W.; validation, A.R. and A.J.; formal analysis, A.J.; investigation, A.R.; resources, A.R. and A.J.; data curation, A.J. and B.W.; writing—original draft preparation, A.J.; writing—review and editing, A.R., D.S., A.J., B.B.-K. and B.W.; visualization, A.J. and B.W.; supervision, B.W.; project administration, B.B.-K.; funding acquisition, A.J., B.B.-K. and B.W. All authors have read and agreed to the published version of the manuscript.

Funding: This research was co-funded by "Excellence Initiative—Research University (2020–2026)" under the programme of the Ministry of Science and Higher Education of Poland (grant number 501-D312-20-0004316).

Institutional Review Board Statement: The animal study protocol was approved by the Ethics Committee of Medical University of Warsaw (protocol code 45/2014, date of approval 15 April 2014).

Informed Consent Statement: Not applicable.

Data Availability Statement: The data presented in this study are available on request from the corresponding author. The data are not publicly available due to the privacy issues.

Conflicts of Interest: The authors declare no conflict of interest.

References

1. Siegel, R.L.; Miller, K.D.; Jemal, A. Cancer statistics, 2020. *CA Cancer J. Clin.* **2020**, *70*, 7–30. [CrossRef] [PubMed]
2. Siegel, R.L.; Miller, K.D.; Fuchs, H.E.; Jemal, A. Cancer Statistics, 2021. *CA Cancer J. Clin.* **2021**, *71*, 7–33. [CrossRef] [PubMed]
3. Smith, C.J.; Minas, T.Z.; Ambs, S. Analysis of Tumor Biology to Advance Cancer Health Disparity Research. *Am. J. Pathol.* **2018**, *188*, 304–316. [CrossRef] [PubMed]
4. Panigrahi, G.K.; Praharaj, P.P.; Kittaka, H.; Mridha, A.R.; Black, O.M.; Singh, R.; Mercer, R.; van Bokhoven, A.; Torkko, K.C.; Agarwal, C.; et al. Exosome proteomic analyses identify inflammatory phenotype and novel biomarkers in African American prostate cancer patients. *Cancer Med.* **2019**, *8*, 1110–1113. [CrossRef] [PubMed]
5. Frattaroli, J.; Weidner, G.; Dnistrian, A.M.; Kemp, C.; Daubenmier, J.J.; Marlin, R.O.; Crutchfield, L.; Yglecias, L.; Carroll, P.R.; Ornish, D. Clinical Events in Prostate Cancer Lifestyle Trial: Results From Two Years of Follow-Up. *Urology* **2008**, *72*, 1319–1323. [CrossRef]
6. Patel, V.H. Nutrition and prostate cancer: An overview. *Expert Rev. Anticancer Ther.* **2014**, *14*, 1295–1304. [CrossRef]
7. Aune, D.; Navarro Rosenblatt, D.A.; Chan, D.S.; Vieira, A.R.; Vieira, R.; Greenwood, D.C.; Vatten, L.J.; Norat, T. Dairy products, calcium, and prostate cancer risk: A systematic review and meta-analysis of cohort studies. *Am. J. Clin. Nutr.* **2015**, *101*, 87–117. [CrossRef]
8. Lippman, S.M.; Klein, E.A.; Goodman, P.J.; Lucia, M.S.; Thompson, I.M.; Ford, L.G.; Parnes, H.L.; Minasian, L.M.; Gaziano, J.M.; Hartline, J.A.; et al. Effect of Selenium and Vitamin E on Risk of Prostate Cancer and Other Cancers. *JAMA* **2009**, *301*, 39. [CrossRef]

9. Swami, S.; Krishnan, A.V.; Feldman, D. Vitamin D Metabolism and Action in the Prostate: Implications for Health and Disease. *Mol. Cell. Endocrinol.* **2011**, *347*, 61–69. [CrossRef]
10. Gregg, J.R.; Zheng, J.; Lopez, D.S.; Reichard, C.; Browman, G.; Chapin, B.; Kim, J.; Davis, J.; Daniel, C.R. Diet quality and Gleason grade progression among localised prostate cancer patients on active surveillance. *Br. J. Cancer* **2019**, *120*, 466–471. [CrossRef]
11. Costello, L.C.; Franklin, R.B. A comprehensive review of the role of zinc in normal prostate function and metabolism; and its implications in prostate cancer. *Arch. Biochem. Biophys.* **2016**, *611*, 100–112. [CrossRef] [PubMed]
12. Nyman, D.W.; Stratton, M.S.; Kopplin, M.J.; Dalkin, B.L.; Nagle, R.B.; Gandolfi, A.J. Selenium and selenomethionine levels in prostate cancer patients. *Cancer Detect. Prev.* **2004**, *28*, 8–16. [CrossRef] [PubMed]
13. Doble, P.A.; Miklos, G.L.G. Distributions of manganese in diverse human cancers provide insights into tumour radioresistance. *Metallomics* **2018**, *10*, 1191–1210. [CrossRef] [PubMed]
14. Bishop, D.P.; Clases, D.; Fryer, F.; Williams, E.; Wilkins, S.; Hare, D.J.; Cole, N.; Karst, U.; Doble, P.A. Elemental bio-imaging using laser ablation-triple quadrupole-ICP-MS. *J. Anal. At. Spectrom.* **2016**, *31*, 197–202. [CrossRef]
15. Kiziler, A.R.; Aydemir, B.; Guzel, S.; Alici, B.; Ataus, S.; Tuna, M.B.; Durak, H.; Kilic, M. May the level and ratio changes of trace elements be utilized in identification of disease progression and grade in prostatic cancer? *Trace Elem. Electrolytes* **2010**, *27*, 65–72. [CrossRef]
16. Zaichick, V.; Zaichick, S. Use of INAA and ICP-MS for the assessment of trace element mass fractions in adult and geriatric prostate. *J. Radioanal. Nucl. Chem.* **2014**, *301*, 383–397. [CrossRef]
17. Zaichick, V.; Zaichick, S. Ratios of Cadmium/Trace Element Contents in Prostate Gland as Carcinoma's Markers. *Canc. Ther. Oncol. Int. J.* **2017**. [CrossRef]
18. Leitão, R.G.; Palumbo, A.; Souza, P.A.V.R.; Pereira, G.R.; Canellas, C.G.L.; Anjos, M.J.; Nasciutti, L.E.; Lopes, R.T. Elemental concentration analysis in prostate tissues using total reflection X-ray fluorescence. *Radiat. Phys. Chem.* **2014**, *95*, 62–64. [CrossRef]
19. Singh, B.P.; Dwivedi, S.; Dhakad, U.; Murthy, R.C.; Choubey, V.K.; Goel, A.; Sankhwar, S.N. Status and Interrelationship of Zinc, Copper, Iron, Calcium and Selenium in Prostate Cancer. *Indian J. Clin. Biochem.* **2016**, *31*, 50–56. [CrossRef]
20. Vinceti, M.; Venturelli, M.; Sighinolfi, C.; Trerotoli, P.; Bonvicini, F.; Ferrari, A.; Bianchi, G.; Serio, G.; Bergomi, M.; Vivoli, G. Case-control study of toenail cadmium and prostate cancer risk in Italy. *Sci. Total Environ.* **2007**, *373*, 77–81. [CrossRef]
21. Daragó, A.; Sapota, A.; Nasiadek, M.; Klimczak, M.; Kilanowicz, A. The effect of zinc and selenium supplementation mode on their bioavailability in the rat prostate. Should administration be joint or separate? *Nutrients* **2016**, *8*, 601. [CrossRef] [PubMed]
22. Ng, K.H.; Bradley, D.A.; Looi, L.M. Elevated trace element concentrations in malignant breast tissues. *Br. J. Radiol.* **1997**, *70*, 375–382. [CrossRef] [PubMed]
23. Durak, I.; Kavutcu, M.; Canbolat, O.; Işik, A.U.; Akyol, O. Concentrations of some major and minor elements in larynx tissues with and without cancer. *Biometals* **1994**, *7*, 45–48. [CrossRef] [PubMed]
24. Dai, Q.; Motley, S.S.; Smith, J.A.; Concepcion, R.; Barocas, D.; Byerly, S.; Fowke, J.H. Blood magnesium, and the interaction with calcium, on the risk of high-grade prostate cancer. *PLoS ONE* **2011**, *6*, e18237. [CrossRef] [PubMed]
25. Al-Ebraheem, A.; Farquharson, M.J.; Ryan, E. The evaluation of biologically important trace metals in liver, kidney and breast tissue. *Appl. Radiat. Isot.* **2009**, *67*, 470–474. [CrossRef] [PubMed]
26. Christudoss, P.; Selvakumar, R.; Fleming, J.J.; Gopalakrishnan, G. Zinc status of patients with benign prostatic hyperplasia and prostate carcinoma. *Indian J. Urol.* **2011**, *27*, 14–18. [CrossRef]
27. Sapota, A.; Daragó, A.; Taczalski, J.; Kilanowicz, A. Disturbed homeostasis of zinc and other essential elements in the prostate gland dependent on the character of pathological lesions. *BioMetals* **2009**, *22*, 1041–1049. [CrossRef] [PubMed]
28. Zachara, B.A.; Marchaluk-Wiśniewska, E.; Maciag, A.; Pepliński, J.; Skokowski, J.; Lambrecht, W. Decreased selenium concentration and glutathione peroxidase activity in blood and increase of these parameters in malignant tissue of lung cancer patients. *Lung* **1997**, *175*, 321–332. [CrossRef] [PubMed]
29. Cai, X.; Wang, C.; Yu, W.; Fan, W.; Wang, S.; Shen, N.; Wu, P.; Li, X.; Wang, F. Selenium Exposure and Cancer Risk: An Updated Meta-analysis and Meta-regression. *Sci. Rep.* **2016**, *6*, 19213. [CrossRef]
30. Yu, S.-Y.; Chu, Y.-J.; Gong, X.-L.; Hou, C.; Li, W.-G.; Gong, H.-M.; Xie, J.-R. Regional variation of cancer mortality incidence and its relation to selenium levels in China. *Biol. Trace Elem. Res.* **1985**, *7*, 21–29. [CrossRef]
31. Daragó, A.; Sapota, A.; Duda-Szymańska, J. Levels of cadmium, zinc, copper and selenium in subjects with diagnosed prostate cancer. *Rocz. Panstw. Zakl. Hig.* **2003**, *54*, 39–40. [PubMed]
32. Venkateswaran, V.; Fleshner, N.E.; Klotz, L.H. Modulation of cell proliferation and cell cycle regulators by vitamin E in human prostate carcinoma cell lines. *J. Urol.* **2002**, *168*, 1578–1582. [CrossRef]
33. Charalabopoulos, K.; Kotsalos, A.; Batistatou, A.; Charalabopoulos, A.; Vezyraki, P.; Peschos, D.; Kalfakakou, V.; Evangelou, A. Selenium in serum and neoplastic tissue in breast cancer: Correlation with CEA. *Br. J. Cancer* **2006**, *95*, 674–676. [CrossRef]
34. Wolf, A.; Wennemuth, G. Ca2+ clearance mechanisms in cancer cell lines and stromal cells of the prostate. *Prostate* **2014**, *74*, 29–40. [CrossRef] [PubMed]
35. Williams, C.D.; Whitley, B.M.; Hoyo, C.; Grant, D.J.; Schwartz, G.G.; Presti, J.C.; Iraggi, J.D.; Newman, K.A.; Gerber, L.; Taylor, L.A.; et al. Dietary calcium and risk for prostate cancer: A case- control study among US veterans. *Prev. Chronic Dis.* **2012**, *9*, E39. [CrossRef] [PubMed]
36. Skrajnowska, D.; Bobrowska-Korczak, B.; Tokarz, A. Disorders of mechanisms of calcium metabolism control as potential risk factors of prostate cancer. *Curr. Med. Chem.* **2017**, *24*, 4229–4244. [CrossRef] [PubMed]

37. Li, K.; Kaaks, R.; Linseisen, J.; Rohrmann, S. Dietary calcium and magnesium intake in relation to cancer incidence and mortality in a German prospective cohort (EPIC-Heidelberg). *Cancer Causes Control* **2011**, *22*, 1375–1382. [CrossRef]
38. Bonithon-Kopp, C.; Kronborg, O.; Giacosa, A.; Räth, U.; Faivre, J. Calcium and fibre supplementation in prevention of colorectal adenoma recurrence: A randomised intervention trial. *Lancet* **2000**, *356*, 1300–1306. [CrossRef]
39. Banas, A.; Kwiatek, W.M.; Banas, K.; Gajda, M.; Pawlicki, B.; Cichocki, T. Correlation of concentrations of selected trace elements with Gleason grade of prostate tissues. *J. Biol. Inorg. Chem.* **2010**, *15*, 1147–1155. [CrossRef]
40. Ludwig, H.; Evstatiev, R.; Kornek, G.; Aapro, M.; Bauernhofer, T.; Buxhofer-Ausch, V.; Fridrik, M.; Geissler, D.; Geissler, K.; Gisslinger, H.; et al. Iron metabolism and iron supplementation in cancer patients. *Wien. Klin. Wochenschr.* **2015**, *127*, 907–919. [CrossRef]
41. Torti, S.V.; Torti, F.M. Iron and cancer: More ore to be mined. *Nat. Rev. Cancer* **2013**, *13*, 342–355. [CrossRef] [PubMed]
42. Cheng, Z.; Dai, L.L.; Song, Y.N.; Kang, Y.; Si, J.M.; Xia, J.; Liu, Y.F. Regulatory effect of iron regulatory protein-2 on iron metabolism in lung cancer. *Genet. Mol. Res.* **2014**, *13*, 5514–5522. [CrossRef] [PubMed]
43. Järup, L. Hazards of heavy metal contamination. *Br. Med. Bull.* **2003**, *68*, 167–182. [CrossRef] [PubMed]
44. Theophanides, T.; Anastassopoulou, J. Copper and carcinogenesis. *Crit. Rev. Oncol. Hematol.* **2002**, *42*, 57–64. [CrossRef]
45. Denoyer, D.; Clatworthy, S.A.S.; Masaldan, S.; Meggyesy, P.M.; Cater, M.A. Heterogeneous copper concentrations in cancerous human prostate tissues. *Prostate* **2015**, *75*, 1510–1517. [CrossRef]
46. Rao, S.S.; Lago, L.; Gonzalez De Vega, R.; Bray, L.; Hare, D.J.; Clases, D.; Doble, P.A.; Adlard, P.A. Characterising the spatial and temporal brain metal profile in a mouse model of tauopathy. *Metallomics* **2020**, *12*, 301–313. [CrossRef]
47. Matusch, A.; Depboylu, C.; Palm, C.; Wu, B.; Höglinger, G.U.; Schäfer, M.K.H.; Becker, J.S. Cerebral Bioimaging of Cu, Fe, Zn, and Mn in the MPTP Mouse Model of Parkinson's Disease Using Laser Ablation Inductively Coupled Plasma Mass Spectrometry (LA-ICP-MS). *J. Am. Soc. Mass Spectrom.* **2010**, *21*, 161–171. [CrossRef]
48. Franklin, K.; Paxinos, G. *The Mouse Brain in Stereotaxic Coordinates*; Academic Press: Cambridge, MA, USA, 2001; ISBN 9780123742445.
49. Opačić, M.; Ristić, A.J.; Sokić, D.; Baščarević, V.; Raičević, S.; Savić, S.; Zorović, M.; Živin, M.; Simon, V.; Spasojević, I.; et al. Regional distribution of cytochrome c oxidase activity and copper in sclerotic hippocampi of epilepsy patients. *Brain Behav.* **2020**, *11*, e01986. [CrossRef]
50. Duvernoy, H.M.; Cattin, F.; Risold, P.-Y. *The Human Hippocampus Functional Anatomy, Vascularization and Serial Sections with MRI*, 3rd ed.; Springer International Publishing: New York, NY, USA, 2005.
51. Fingerhut, S.; Sperling, M.; Holling, M.; Niederstadt, T.; Allkemper, T.; Radbruch, A.; Heindel, W.; Paulus, W.; Jeibmann, A.; Karst, U. Gadolinium-based contrast agents induce gadolinium deposits in cerebral vessel walls, while the neuropil is not affected: An autopsy study. *Acta Neuropathol.* **2018**, *136*, 127–138. [CrossRef]
52. Theiner, S.; Schweikert, A.; Van Malderen, S.J.M.; Schoeberl, A.; Neumayer, S.; Jilma, P.; Peyrl, A.; Koellensperger, G. Laser Ablation-Inductively Coupled Plasma Time-of-Flight Mass Spectrometry Imaging of Trace Elements at the Single-Cell Level for Clinical Practice. *Anal. Chem.* **2019**, *91*, 8207–8212. [CrossRef]
53. Kamaly, N.; Pugh, J.A.; Kalber, T.L.; Bunch, J.; Miller, A.D.; McLeod, C.W.; Bell, J.D. Imaging of gadolinium spatial distribution in tumor tissue by laser ablation inductively coupled plasma mass spectrometry. *Mol. Imaging Biol.* **2010**, *12*, 361–366. [CrossRef] [PubMed]
54. Radbruch, A.; Richter, H.; Fingerhut, S.; Martin, L.F.; Xia, A.; Henze, N.; Paulus, W.; Sperling, M.; Karst, U.; Jeibmann, A. Gadolinium Deposition in the Brain in a Large Animal Model: Comparison of Linear and Macrocyclic Gadolinium-Based Contrast Agents. *Invest. Radiol.* **2019**, *54*, 531–536. [CrossRef] [PubMed]
55. Bücker, P.; Richter, H.; Radbruch, A.; Sperling, M.; Brand, M.; Holling, M.; Van Marck, V.; Paulus, W.; Jeibmann, A.; Karst, U. Deposition patterns of iatrogenic lanthanum and gadolinium in the human body depend on delivered chemical binding forms. *J. Trace Elem. Med. Biol.* **2021**, *63*, 126665. [CrossRef] [PubMed]
56. Uca, Y.O.; Hallmann, D.; Hesse, B.; Seim, C.; Stolzenburg, N.; Pietsch, H.; Schnorr, J.; Taupitz, M. Microdistribution of Magnetic Resonance Imaging Contrast Agents in Atherosclerotic Plaques Determined by LA-ICP-MS and SR-μXRF Imaging. *Mol. Imaging Biol.* **2021**, *23*, 382–393. [CrossRef] [PubMed]
57. Sajnóg, A.; Hanć, A.; Barałkiewicz, D.; Gryszczyńska, B.; Majewski, W.; Iskra, M. Bioimaging of macro- and microelements in blood vessels with calcified plaque in atherosclerosis obliterans by LA-ICP-MS. *Microchem. J.* **2019**, *150*, 104090. [CrossRef]
58. M-M, P.; Weiskirchen, R.; Gassler, N.; Bosserhoff, A.K.; Becker, J.S. Novel Bioimaging Techniques of Metals by Laser Ablation Inductively Coupled Plasma Mass Spectrometry for Diagnosis Of Fibrotic and Cirrhotic Liver Disorders. *PLoS ONE* **2013**, *8*, e58702. [CrossRef]
59. Pornwilard, M.M.; Merle, U.; Weiskirchen, R.; Becker, J.S. Bioimaging of copper deposition in Wilson's diseases mouse liver by laser ablation inductively coupled plasma mass spectrometry imaging (LA-ICP-MSI). *Int. J. Mass Spectrom.* **2013**, *354–355*, 281–287. [CrossRef]
60. Castellanos-García, L.J.; Gokhan Elci, S.; Vachet, R.W. Reconstruction, analysis, and segmentation of LA-ICP-MS imaging data using Python for the identification of sub-organ regions in tissues. *Analyst* **2020**, *145*, 3705–3712. [CrossRef]
61. Osterholt, T.; Salber, D.; Matusch, A.; Becker, J.S.; Palm, C. IMAGENA: Image Generation and Analysis—An interactive software tool handling LA-ICP-MS data. *Int. J. Mass Spectrom.* **2011**, *307*, 232–239. [CrossRef]

62. Halbach, K.; Holbrook, T.; Reemtsma, T.; Wagner, S. Effective processing and evaluation of chemical imaging data with respect to morphological features of the zebrafish embryo. *Anal. Bioanal. Chem.* **2021**, *413*, 1675–1687. [CrossRef]
63. Lee, R.F.S.; Theiner, S.; Meibom, A.; Koellensperger, G.; Keppler, B.K.; Dyson, P.J. Application of imaging mass spectrometry approaches to facilitate metal-based anticancer drug research. *Metallomics* **2017**, *9*, 365–381. [CrossRef] [PubMed]
64. Becker, J.S.; Matusch, A.; Wu, B. Bioimaging mass spectrometry of trace elements—recent advance and applications of LA-ICP-MS: A review. *Anal. Chim. Acta* **2014**, *835*, 1–18. [CrossRef] [PubMed]
65. Matusch, A.; Bauer, A.; Becker, J.S. Element imaging in formalin fixed slices of human mesencephalon. *Int. J. Mass Spectrom.* **2011**, *307*, 240–244. [CrossRef]
66. Becker, J.S.; Breuer, U.; Hsieh, H.F.; Osterholt, T.; Kumtabtim, U.; Wu, B.; Matusch, A.; Caruso, J.A.; Qin, Z. Bioimaging of metals and biomolecules in mouse heart by laser ablation inductively coupled plasma mass spectrometry and secondary ion mass spectrometry. *Anal. Chem.* **2010**, *82*, 9528–9533. [CrossRef] [PubMed]
67. Oros-Peusquens, A.M.; Matusch, A.; Becker, J.S.; Shah, N.J. Automatic segmentation of tissue sections using the multielement information provided by LA-ICP-MS imaging and k-means cluster analysis. *Int. J. Mass Spectrom.* **2011**, *307*, 245–252. [CrossRef]
68. Jagielska, A.; Ruszczyńska, A.; Wagner, B.; Bulska, E.; Skrajnowska, D.; Bobrowska-Korczak, B. ICP-MS analysis of diet supplementation influence on the elemental content of rat prostate gland. *Mon. Chem. Chem. Mon.* **2019**, *150*, 1681–1690. [CrossRef]
69. Jagielska, A.; Ruszczyńska, A.; Bulska, E.; Wagner, B. The impact of sample preparation on the elemental composition of soft tissues assessed by laser ablation ICP-MS. *J. Anal. At. Spectrom.* **2020**. [CrossRef]
70. Currie, L.A. Nomenclature in evaluation of analytical methods including detection and quantification capabilities. *Pure Appl. Chem.* **1995**, *36*, T189–T195. [CrossRef]
71. Wagner, B.; Czajka, A. Non-invasive approximation of elemental composition of historic inks by LA-ICP-MS measurements of bathophenanthroline indicators. *Talanta* **2021**, *222*, 121520. [CrossRef]
72. Singh, C.K.; Pitschmann, A.; Ahmad, N. Resveratrol-zinc combination for prostate cancer management. *Cell Cycle* **2014**, *13*, 1867–1874. [CrossRef]
73. Costello, L.C.; Franklin, R.B. The clinical relevance of the metabolism of prostate cancer; zinc and tumor suppression: Connecting the dots. *Mol. Cancer* **2006**, *5*, 17. [CrossRef]
74. Krone, C.A.; Harms, L.C.; Leitzmann, M.F.; Giovannucci, E.L. Re: Zinc supplement use and risk of prostate cancer. *J. Natl. Cancer Inst.* **2003**, *95*, 1556–1557. [CrossRef] [PubMed]
75. Kolenko, V.; Teper, E.; Kutikov, A.; Uzzo, R. Zinc and zinc transporters in prostate carcinogenesis. *Nat. Rev. Urol.* **2013**, *10*, 219–226. [CrossRef]
76. Sapota, A.; Daragó, A.; Skrzypińska-Gawrysiak, M.; Nasiadek, M.; Klimczak, M.; Kilanowicz, A. The bioavailability of different zinc compounds used as human dietary supplements in rat prostate: A comparative study. *Biometals* **2014**, *27*, 495–505. [CrossRef] [PubMed]
77. John, E.; Laskow, T.C.; Buchser, W.J.; Pitt, B.R.; Basse, P.H.; Butterfield, L.H.; Kalinski, P.; Lotze, M.T. Zinc in innate and adaptive tumor immunity. *J. Transl. Med.* **2010**, *8*, 118. [CrossRef] [PubMed]
78. Ho, E. Zinc deficiency, DNA damage and cancer risk. *J. Nutr. Biochem.* **2004**, *15*, 572–578. [CrossRef] [PubMed]
79. Sainburg, T.; McInnes, L.; Gentner, T.Q. Parametric umap embeddings for representation and semisupervised learning. *Neural Comput.* **2021**, *33*, 2881–2907. [CrossRef]
80. Lukmanov, R.A.; Riedo, A.; Wacey, D.; Ligterink, N.F.W.; Grimaudo, V.; Tulej, M.; de Koning, C.; Neubeck, A.; Wurz, P. On Topological Analysis of fs-LIMS Data. Implications for in Situ Planetary Mass Spectrometry. *Front. Artif. Intell.* **2021**, *4*, 668163. [CrossRef]